Journal of Marine Research, 49, 635–658, 1991

Modeling of internal tides in fjords

by V. Tverberg[1,2], B. Cushman-Roisin[3] and H. Svendsen[1]

ABSTRACT

A previous model for the distribution of internal tides above irregular topography is generalized to include arbitrary stratification and a radiation condition at the open boundary. Thanks to a small amount of dissipation, this model remains valid in the presence of resonant internal tides, leading to intense wave-energy beams.

An application to a Norwegian fjord correctly reproduces the observed energy pattern consisting of two beams both originating at the 60-meter deep entrance sill and extending in-fjord, one upward toward the surface, the other downward toward the bottom. After correction for the varying width of the fjord, the observed and modelled energy levels are in good agreement, especially in the upper levels where energy is the greatest. Furthermore, the substantial phase lag between these two energy beams revealed by the observations is correctly reproduced by the model. Finally, a third and very narrow energy spike is noted in the model at the level of a secondary bump inward of the sill. This beam is missed by the current meter data, because the current meters were placed only at a few selected depths. But an examination of the salinity profiles reveals a mixed layer at approximately the same depth. The explanation is that high-wave energy leads to wave breaking and vigorous mixing.

The model's greatest advantage is to provide the internal-tide energy distribution throughout the fjord. Discrepancies between observations and model are attributed to coarse vertical resolution in the vicinity of the sill and to unaccounted cross-fjord variations.

1. Introduction

A primary generation mechanism of internal waves in the ocean is the interaction of the tide with topographic features. The situation arises when the open-ocean surface tide encounters the shelf break (Rattray, 1960; Prinsenberg and Rattray, 1975; deWitt *et al.,* 1986; Pingree and New, 1989) or a seamount protruding into the main thermocline (Golubev and Cherkesov, 1986). The propagation of the internal-tide energy from its place of origin is further affected by topographic irregularities. For example, Gardner (1989) recently demonstrated that a pronounced focusing of internal tides is responsible for the observed resuspension of sediments in the Baltimore Canyon.

1. Geophysical Institute, Avd. A, University of Bergen, Allégaten 70, Bergen, Norway.
2. Present address: Bedford Institute of Oceanography, P.O. Box 1006, Dartmouth, N.S., Canada, B2Y 4A2.
3. Thayer School of Engineering, Dartmouth College, Hanover, New Hampshire, 03755, U.S.A.

Norwegian fjords are prime sites of energetic internal waves. Indeed, not only are they located along the North Atlantic Ocean where the tide is relatively large, but their morphology marked by steep sills and abrupt slopes is also critical in generating and diffracting internal tides. Since large internal waves lead to wave breaking and wave breaking to mixing and dispersion of nutrients, the determination of the internal-tide energy distribution is particularly important in Norwegian fjords where aquaculture is extensive.

Traditional models can be classified in two categories. One class exploits the technique of vertical-mode decomposition (Prinsenberg and Rattray, 1975; New, 1988; Pingree and New, 1989). Because vertical modes strictly exist only over horizontal portions of the bottom, the topography in these models is restricted to consist of only a few steps. Other traditional models (Wunsch, 1969; Baines, 1971, 1974; Sandstrom, 1976) and more recent applications (Craig, 1987; Vlasenko, 1987) have taken advantage of the hyperbolic nature of the problem to obtain solutions via a ray-tracing technique of one form or another. But, this approach typically requires the construction of a rule or matrix relating the various reflection points along a series of rays and becomes extremely cumbersome in the case of arbitrary topography. This is why the above models are applicable only to systems with subcritical slopes, with monotonic slopes or without facing supercritical slopes. Such restrictions also avoid eventual cases of resonance, which may be quite common (Lewis and Perkin, 1982; de Young and Pond, 1987). Breaking with this tradition are the finite-difference models of Chuang and Wang (1981) and Cushman-Roisin *et al.* (1989, hereafter referred to as CRTP). The former relies on a change of coordinates that transforms the domain into a rectangle, which is subsequently divided along evenly spaced grid points. In addition to the contamination of the results caused by the discretization of mapping factors in such models (McCalpin, 1990), the transformation of coordinate involves the second derivative of the bottom profile. It follows that applications must be restricted to bottom topographies with smooth profiles or with known analytic expressions. The other, CRTP model overcomes these difficulties by solving the problem on a rectangular grid in real space with the mesh diagonals chosen to be aligned with the ray directions. The uneven bottom is replaced by a stepped boundary that best approximates the actual topography, and the hyperbolic system is converted into a parabolic set of equations amenable to a convenient iterative method of solution. Furthermore, a dissipation term is introduced to overcome eventual resonance. The advantages of this model are its ease of application to arbitrary bottom topographies and its allowance for resonant patterns.

A fourth approach to the simulation of internal tides is to solve the time-dependent primitive equations directly. The main advantage is the allowance for nonlinear effects, such as the advection of internal waves by the oscillating currents of the surface tide (Hibiya, 1986). In addition to a greater computer demand (which translates into lower resolution), the need to specify proper open-boundary condi-

tions is problematic. The specification of the streamfunction according to the incoming surface tide (Hibiya, 1988) effectively reflects all internal modes and may contaminate the entire solution, especially if the system is near resonance as is the case of shallow-sill fjords.

In the original version (Cushman-Roisin *et al.,* 1989), the CRTP model was presented in its simplest form. Namely, the condition at the open boundary where the surface tide enters the system did not allow outgoing internal-wave radiation but instead reflected all internal waves, and the stratification was assumed uniform (constant Brunt-Väisälä frequency). In a nonuniform stratification, rays are refracted (Lighthill, 1978, Section 4.5) and their travel times and points of reflection are thus modified. [In the extreme case of a Brunt-Väisälä frequency dropping below the tidal frequency such as at the base of a mixed layer, internal reflection occurs (Cushman-Roisin and Svendsen, 1983).] Applications of the model to actual oceanic systems obviously require that both of the above restrictions be lifted, and one objective of the present paper is to do so.

The model extension proceeds by steps. First, the radiation boundary condition is discussed in the case of uniform stratification for mathematical convenience. Then, in the case of nonuniform stratification, a stretching of the vertical variable is performed to align the diagonals of the rectangular grid with the local ray slopes. [This vertical stretching is horizontally uniform and avoids the error contamination discussed by McCalpin (1990).] Finally, the radiation boundary condition is revised and implemented in the general case of nonuniform stratification.

After these modifications are implemented (Section 2), the model is applied to the Skjomen fjord. A description of this fjord of North Norway and of the available data is presented in Section 3, while the application of the model and the comparison of the results with the data follow in Section 4. A high-energy layer revealed by the model but missed by the current meter data (taken at other depths) is found to correspond to a zone of mixing reflected in the erosion of the salinity profile. This and other conclusions are summarized in Section 5.

2. The numerical model and its generalizations

a. The basic numerical model. The model developed in CRTP deals with tide-generated internal gravity waves in a linearly stratified fluid without rotation. The tidal frequency ω sets the time dependence of the problem (proportional to $\exp(-i\omega t)$) and the classic equation for the streamfunction ψ

$$\frac{\partial^2\psi}{\partial x^2} - c^2\frac{\partial^2\psi}{\partial z^2} = 0 \tag{1}$$

then describes the wave amplitude distribution. The coefficient $c = \omega/N$, where N is the constant Brunt-Väisälä frequency, defines the characteristic directions $\pm c$ of this hyperbolic equation.

After replacement of ψ by the velocity components, $u = -\partial\psi/\partial z$ and $w = \partial\psi/\partial x$, and scaling of the variables (x by $1/c$, w by c), Eq. (1) is then expressed into two equations

$$\frac{\partial u}{\partial x} + \frac{\partial w}{\partial z} = 0, \frac{\partial u}{\partial z} + \frac{\partial w}{\partial x} = 0 \tag{2a,b}$$

The characteristic slopes are now ± 1. Note that despite scaling, dimensions have been retained. Next, an additional term related to vertical friction is introduced to overcome singularities brought on by eventual resonance:

$$\frac{\partial u}{\partial x} + \frac{\partial w}{\partial z} = 0, \frac{\partial u}{\partial z} + \frac{\partial w}{\partial x} = i\lambda \frac{\partial^3 u}{\partial z^3}, \tag{3a,b}$$

where i is the imaginary unit and $\lambda = \nu/\omega$ is a real, positive constant proportional to the vertical viscosity ν. To avoid a general diffusive effect on the waves, $\lambda \ll H_o^2$ is required, where H_o is a typical depth of the domain.

Finally, Eqs. (3a,b) are transformed into a time-dependent dissipative system, the solution of which evolves from any arbitrary velocity field to a steady-state solution that satisfies (3a,b). To form the numerical system, two accessory functions are introduced:

$$\chi = \frac{\partial u}{\partial x} + \frac{\partial w}{\partial z}, \phi = \frac{\partial u}{\partial z} + \frac{\partial w}{\partial x} - i\lambda \frac{\partial^3 u}{\partial z^3}, \tag{4a,b}$$

and the two dissipative equations that complete the system with four unknowns and four equations are:

$$\frac{\partial u}{\partial t} = \frac{\partial \chi}{\partial x} + \frac{\partial \phi}{\partial z}, \quad \frac{\partial w}{\partial t} = \frac{\partial \chi}{\partial z} + \frac{\partial \phi}{\partial x} + i\lambda \frac{\partial^3 \chi}{\partial z^3}. \tag{4c,d}$$

The steady-state solution of (4a–d) satisfies (3a,b) if $\chi = \phi = 0$ (Cushman-Roisin *et al.*, 1989). For numerical reasons, it is convenient to use a staggered grid on which the characteristic directions follow the diagonals.

Resonance occurs in regions where complicated topographic features make the characteristic rays close, after several reflections, onto themselves. If it were not for the presence of the dissipative term, resonance would be manifested by infinite values of u and w in the original problem (2a,b) or by nonzero residual values of χ and ϕ in the steady-state solution of (*4a–d*) (Cushman-Roisin *et al.*, 1989).

The physical boundary conditions are easily implemented by letting horizontal boundaries pass through w-grid points and vertical boundaries through u-grid points so that the solid boundary conditions become $w = 0$ and $u = 0$, respectively. Along the surface, the forcing from the external tide is implemented by setting the w-values

to a constant (Craig, 1987). More precisely, if the surface elevation at the fjord entrance obeys $\eta = A \sin \omega t$, the vertical velocity at the surface is $A\omega \cos \omega t$, which takes the form $w = A\omega$ in the present notation. Then, because the wavelength of the surface tide is generally much longer than the fjord, this value can be taken uniformly along the fjord. In the CRTP model, the boundary condition at the fjord entrance required that the vertical velocity be equal to that of the external tide, namely linear in z. Such boundary condition reflects the internal waves generated within the domain. All the boundary conditions of χ and ϕ are set to zero. The supplementary boundary conditions required by the higher-order friction term are imposed as a nonstress condition $u_z = 0$ at the surface, and a nonslip condition $u = 0$ along horizontal sections of the topography.

b. Radiation boundary condition with constant N^2. The reason for introducing a radiation condition at the entrance of the domain is to permit the outward propagation of the internal waves generated within the domain. This is done by adjusting the boundary values to an analytical solution outside the entrance.

In the absence of any other information, it is assumed that the bottom outside the domain is flat, with depth equal to that at the entrance, denoted H, and the analytical method of normal modes can be used. Viscosity is not considered because resonance is prohibited over a flat bottom, and thus the λ terms remain small there. So, the equations to be solved in the outer domain are (2a,b).

If the inner domain of interest extends from the entrance in the positive x-direction, the baroclinic mode solutions of (2a,b) containing only outgoing internal waves in the negative x-direction are

$$u_n = \cos\left(\frac{n\pi z}{H}\right) \exp\left(-i\frac{n\pi x}{H}\right) \text{ and } w_n = i \sin\left(\frac{n\pi z}{H}\right) \exp\left(-i\frac{n\pi x}{H}\right)$$

where n is a nonzero integer. Note that this solution satisfies not only the continuous, partial-differential equations but also the second-order centered-difference equations on the staggered grid. The grid-mesh only limits the number of baroclinic modes that can be resolved. This number is equal to the number of w-grid points in the vertical excluding those on the boundaries, say N-1.

Under the long-wavelength approximation for the external tide (Craig, 1987), the barotropic mode has a simple structure: u is independent of depth and linear in x, while w is independent of x and varies linearly with depth from zero at the bottom to the tidal amplitude, say 1, at the surface ($z = H$). The total outer solution (sum of the barotropic and all possible outgoing baroclinic modes) is thus

$$u = u_o - \frac{x}{H} + \sum_{n=1}^{N-1} a_n \cos\left(\frac{n\pi z}{H}\right) \exp\left(-i\frac{n\pi x}{H}\right) \tag{5a}$$

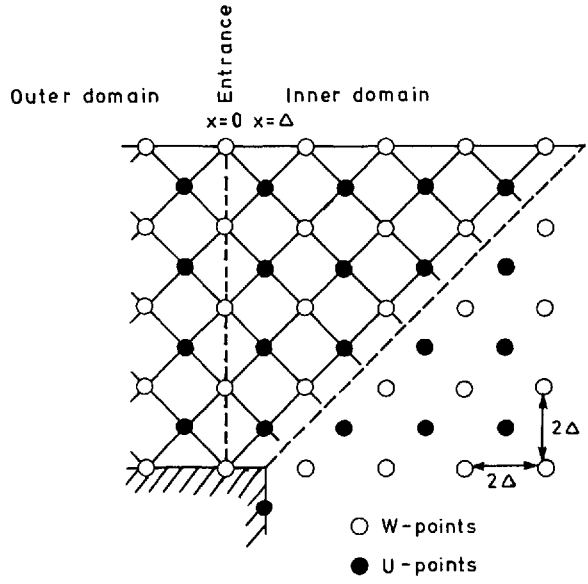

Figure 1. The entrance area of the numerical domain, showing the region of the inner domain where the outer solution is still valid.

$$w = \frac{z}{H} + i \sum_{n=1}^{N-1} a_n \sin\left(\frac{n\pi z}{H}\right) \exp\left(-i \frac{n\pi x}{H}\right). \tag{5b}$$

Consider now the entrance area as depicted in Figure 1. The above solution constructed to represent the wave field in the outer domain (left of $x = 0$, where the bottom is flat) is also valid on the other side inside the triangular domain defined by the entrance boundary, the surface and the diagonal ray extending from the bottom at the entrance to the surface. Indeed, every point in this triangle can be connected by two rays to the entrance line and hence the solution there is completely determined by the outer solution. In particular, the u-values along the first column inside the domain obey (5a).

The procedure now is to make use of these $u_{1j} = u(x = \Delta, z = 2j\Delta - \Delta)$ values to express the $w_{ok} = w(x = 0, z = 2k\Delta)$ values along the entrance, where $\Delta = H/2N$ is the grid step. Eq. (5a) written at $x = \Delta$ and $z = 2j\Delta - \Delta$ with j running from 1 to N yields a set of N equations with N unknowns, viz. u_o and the $N - 1$ values of a_n's. The solution of this set of ordinary linear equations gives the expressions for the a_n's:

$$a_n = \frac{2}{N} \exp\left(i \frac{n\pi}{2N}\right) \sum_{j=1}^{N} \left(u_{1j} - u_o + \frac{\Delta}{H}\right) \cos\left[\left(j - \frac{1}{2}\right) \frac{n\pi}{H}\right], \tag{6}$$

where n ranges from 1 to $N - 1$. Since u_o and Δ/H are constants, the corresponding terms yield zero sums. Eq. (5b) written at $x = 0$ and $z = 2k\Delta$ with k running from 1 to $N - 1$ then relates values of w at the entrance to those of u along the first column

within the domain:

$$w_{ok} = \frac{k}{N} + \sum_{j=1}^{N} A_{kj} u_{1j}, \tag{7}$$

where the coefficients

$$A_{kj} = \frac{2i}{N} \sum_{n=1}^{N-1} \exp\left(\frac{in\pi}{2N}\right) \sin\left(\frac{n\pi k}{N}\right) \cos\left(\left(j - \frac{1}{2}\right)\frac{n\pi}{N}\right) \tag{8}$$

can be calculated once and for all.

Eq. (7) can be implemented in the model as the radiation boundary condition at the entrance of the fjord when the Brunt-Väisälä frequency is uniform. In practice, the w-values at the entrance are updated according to (7) between every iteration of Eqs. (4a–d).

c. Arbitrary $N^2(z)$. In an arbitrarily stratified fluid, the coefficient c^2 in Eq. (1) is continuously varying with z. To illustrate clearly how the model can be extended to this more realistic case, the friction term is first excluded from the equations, and one returns to Eq. (1). From this equation, it is readily seen that the characteristic directions of the problem are still $\pm c$. But, the rays are now curves defined by (Lighthill, 1978, Section 4.5)

$$x = x_o \pm \int_o^z \frac{dz'}{c(z')}. \tag{9}$$

This last expression suggests the introduction of a new vertical variable, ζ, defined by $dz/c = d\zeta$ (Craig, 1988). In the x,ζ frame of reference, the characteristics become straight lines of slopes $\pm$ 1, and, when ζ is substituted for z and friction is reintroduced, the governing equations become

$$\frac{\partial u}{\partial x} + \frac{1}{c}\frac{\partial w}{\partial \zeta} = 0, \quad c\frac{\partial u}{\partial \zeta} + \frac{\partial w}{\partial x} = i\lambda \frac{\partial^3 u}{\partial \zeta^3}. \tag{10a,b}$$

The derivation of the dissipative equations is done by applying the operator $\partial/\partial x$ to (10a) and $1/c\ \partial/\partial\zeta$ to (10b) and adding the results to form the first equation, and applying operator $c\ \partial/\partial\zeta$ to (10a) and $\partial/\partial x$ to (10b) and adding to form the second equation. The system of differential equations to be solved in the case of arbitrary $c(\zeta)$ is then

$$\chi = \frac{\partial u}{\partial x} + \frac{1}{c(\zeta)}\frac{\partial w}{\partial \zeta}, \quad \phi = c(\zeta)\frac{\partial u}{\partial \zeta} + \frac{\partial w}{\partial x} - i\lambda \frac{\partial^3 u}{\partial \zeta^3}, \tag{11a,b}$$

$$\frac{\partial u}{\partial t} = \frac{\partial \chi}{\partial x} + \frac{1}{c(\zeta)}\frac{\partial \phi}{\partial \zeta}, \quad \frac{\partial w}{\partial t} = c(\zeta)\frac{\partial \chi}{\partial \zeta} + \frac{\partial \phi}{\partial x} + i\lambda \frac{\partial^3 \chi}{\partial \zeta^3}. \tag{11c,d}$$

In the above equations, the coefficients are $c(\zeta) = \omega/N(\zeta)$ and $\lambda = \nu N_o/\omega^2$ with ω as the tidal frequency, $N(\zeta)$ the Brunt-Väisälä frequency, ν the viscosity parameter, and N_o a mean value of $N(\zeta)$ such that λ is constant. According to CRTP, the viscosity parameter is required to be small ($\nu \ll \omega H_o^2$, where H_o is a typical depth), and this criterion is easily met. A solution of (11a–d) of the form $\exp(\sigma t + imx + in\zeta)$ provides

$$\sigma = -\left[m^2 + n^2 \pm 2mn\sqrt{1 - \left(\frac{n^3\lambda}{2mc} - \frac{dc/d\zeta}{2mc}\right)^2}\right] \tag{12}$$

which has a nonpositive real part. The above system is thus dissipative. Intuitively, it is expected that the discrete version of the problem will be numerically stable as long as the time step is not too large.

d. Radiation boundary condition with arbitrary $N^2(z)$. In the model version with arbitrary varying $N^2(z)$ the radiation boundary condition outlined earlier in this section must be generalized, but a similar procedure can be utilized. The outer baroclinic-mode solutions are now dependent on the stratification. With the discretized form $u(x = j\Delta,\ \zeta = k\Delta) = U_k \exp(-imj\Delta)$ and $w(x = j\Delta,\ \zeta = k\Delta) = W_k \exp(-imj\Delta)$, the discretized form of (10a) yields

$$U_k = -i\frac{W_{k+1} - W_{k-1}}{2c_k \sin m\Delta},$$

and elimination of U_{k+1} and U_{k-1} in the discretized form of (10b) leads, in the absence of friction, to the linear eigenvalue problem of order $N - 1$:

$$\sum_{q=1}^{N-1} B_{pq}W_q = -\mu W_p,\ p = 1 \text{ to } N - 1. \tag{13}$$

Again, $N - 1$ is the number of unknown w-grid points in the vertical column at the entrance, excluding the bottom and surface points. The tridiagonal matrix B consists of ratios of the discrete buoyancy values c_k. The eigenvalues $\mu = 4\sin^2 m\Delta$ yield the set of horizontal wavenumbers m, while the W_p's are the corresponding eigenvectors. The expression for the eigenvalues requires that their values must be real and in the interval $0 \leq \mu \leq 4$, and this criterion is satisfied if the c_k profile is sufficiently smooth. Too large jumps in the discretized profile can lead to prohibitively large eigenvalues.

After finding the $N - 1$ different eigenvalues and eigenvectors corresponding to the different baroclinic modes, the remaining procedure is identical to that in the case of constant c: Add the barotropic mode to all possible outgoing baroclinic modes (see (5a,b)), form the set of ordinary linear equations valid one grid-step within the domain to determine the constants a_n (see (6)) and express the w-values along the entrance in terms of the u-values one grid-step inside the domain (see

(6)–(7)). The result is:

$$w(x = 0, \zeta = 2k\Delta) = \frac{z}{H} + \sum_{j=1}^{N-1} c_{2j}[u(x = \Delta, \zeta = (2j + 1)\Delta) - u(x = \Delta, \zeta = (2j - 1)\Delta)]A_{jk}, \quad (14)$$

for $k = 1$ to $N - 1$, and where the elements

$$A_{jk} = \sum_{n=1}^{N-1} \frac{1}{2}\left[1 - i\sqrt{\frac{4 - \mu_n}{\mu_n}}\right] W_{kn}W_{nj}^{-1} \quad (15)$$

form the generalized matrix A, which can be evaluated once and for all before the model is run. W_{kn} are the elements from the matrix W containing the n normalized eigenvectors, and W_{nj}^{-1} are the elements of the inverse of this matrix.

3. The Skjomen Fjord

a. Fjord characteristics. Skjomen is a sill fjord located near the head of the Vestfjorden-Ofotfjorden fjord system, in the northern part of Norway (Fig. 2). It is oriented approximately north-south with the mouth at the northern end, and is surrounded by steep mountains. The length of the fjord is about 25 km, while the width varies considerably, from 400 meters at the mouth to about 3 km at the widest section. The sill is located a few hundred meters outside the mouth and is flanked by two broad shoulders (Fig. 3). The top of the sill is about 60 meters deep, while depth at the inner shoulder is 87 meters. Inside from the sill, Skjomen has a deep basin, of about 165 meters at its deepest point.

b. Available data. During a research program from 1977 to 1979, current and temperature measurements were made in Skjomen, and these were analyzed with regard to internal tides (Cushman-Roisin and Svendsen, 1983). Two analytical methods, normal modes and ray tracing, were applied to the data, although neither is strictly applicable in this situation. Based on the knowledge acquired by this analysis, an additional sampling program took place during the period of August 4–September 6, 1983. Three current meter moorings were situated at the locations marked M1, M2, and M3 on Figures 2 and 3. Each mooring contained ten Aanderaa current meters (Aanderaa, 1979), recording speed, direction, and temperature every 20 minutes. The observation depths were 5, 10, 15, 20, 40, 60, 80, 100 and 120 meters for all three moorings, and in addition 145 meters for M1 and M2, and 130 meters for M3. All current meters were recording at fixed time intervals: 10, 30, and 50 minutes past the hour. From the recorded speeds and directions, horizontal north-south (in-out fjord) and east-west (transverse) velocity components were calculated.

In addition to these current measurements, hydrographical data were collected near mooring M1 once a week during the observation period. With a MC-4 measuring bridge, salinity and temperature were sampled at 27 selected depths down

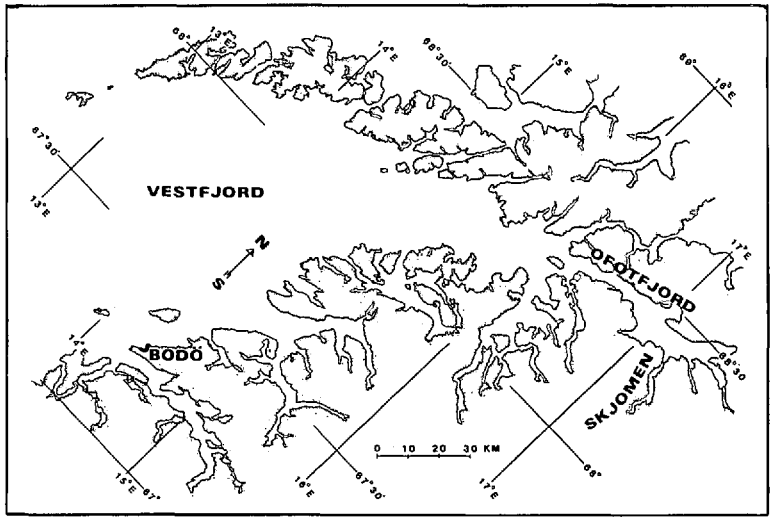

a

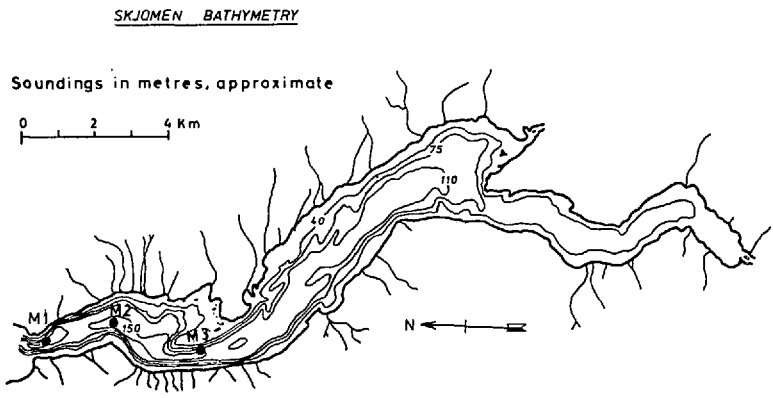

b

Figure 2. (a) Map of Vestfjorden-Ofotfjord and the surrounding fjord system. (b) Map of the Skjomen bathymetry. The soundings are in meters and only approximate. The three moorings are marked M1, M2, and M3.

to 90 meters with intervals ranging from 0.5 m just below the surface to 10 m in the deepest part. From these measurements, density profiles were calculated, and the density profile was seen to remain quite stationary throughout the sampling period, except in the surface layer (<2 m). On the last day of the sampling program, CTD-stations were taken at eleven positions in the fjord. Among them two profiles were taken at the position of mooring M1 at 12:05 (st.99) and 19:05 GMT (st.109), and two near mooring M_2 at 12:20 (st.100) and 18:50 GMT (st.108).

To form hourly time series, a Butterworth low-pass filter with a two-hour cutoff

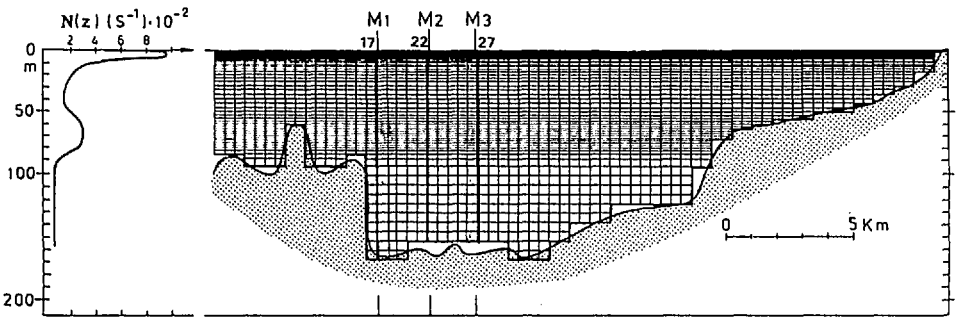

Figure 3. Long-section of the Skjomen fjord, the smooth line shows the actual bottom topography while the stepped line is the model boundary. The Brunt-Väisälä frequency $N(z)$ representative for the sampling period in August 1983 is displayed on the side. The figure also shows the chosen grid mesh for the model run. The positions of the moorings M1, M2, and M3, each containing eleven currentmeters, are indicated. Columns 17, 22 and 27 of the grid (thick vertical lines) contain the u-grid points used for comparison with the moorings data.

was first applied on the original time series, and then one value per hour was extracted to form a time series covering the period from 18:00 hr. August 4 to 24:00 hr. September 1. A tidal analysis of velocity time series following the method of Godin (1972) returned a resolution of more than 30 frequencies. For each frequency, major and minor axes of the corresponding tidal ellipses, their orientation in space, and the Greenwich phase lags were calculated. In all time series, the M_2-tide with a period of 12.42 hours shows by far the clearest signal. Therefore, only waves at that frequency are examined here.

Figure 4 shows the ellipses of the M_2-tide extracted from the time series for every depth and mooring location, and it is seen how the horizontal velocity vector changes magnitude and direction with depth and location as one tidal period unfolds. The ellipses are quite elongated, indicating topographical steering, i.e. the velocities mostly follow the direction of the fjord. More importantly, Figure 4 shows that the energy, related to the major axis of the ellipses, varies both longitudinally and vertically. Later, to display the energy distribution, the major axes of the tidal ellipses will be squared, and the resulting depth profiles will be compared to the model results. But, what is already apparent from the ellipses is a level of minimum energy at about 60 meters depth, the sill level. This is in agreement with the theoretical study of Buckley (1980) concluding that modes with vanishing horizontal velocity at sill depth are preferred.

On every ellipse, a phase lag indicates by how much the local internal tide is shifted compared to the surface tide at the fjord entrance. Because the data positions are fixed in the time series, it is possible to compare the phase lags among time series. For Figures 5a,b, and c, vectors are constructed from the different depths at the three moorings with angles equal to phase lags measured in a right-handed coordinate

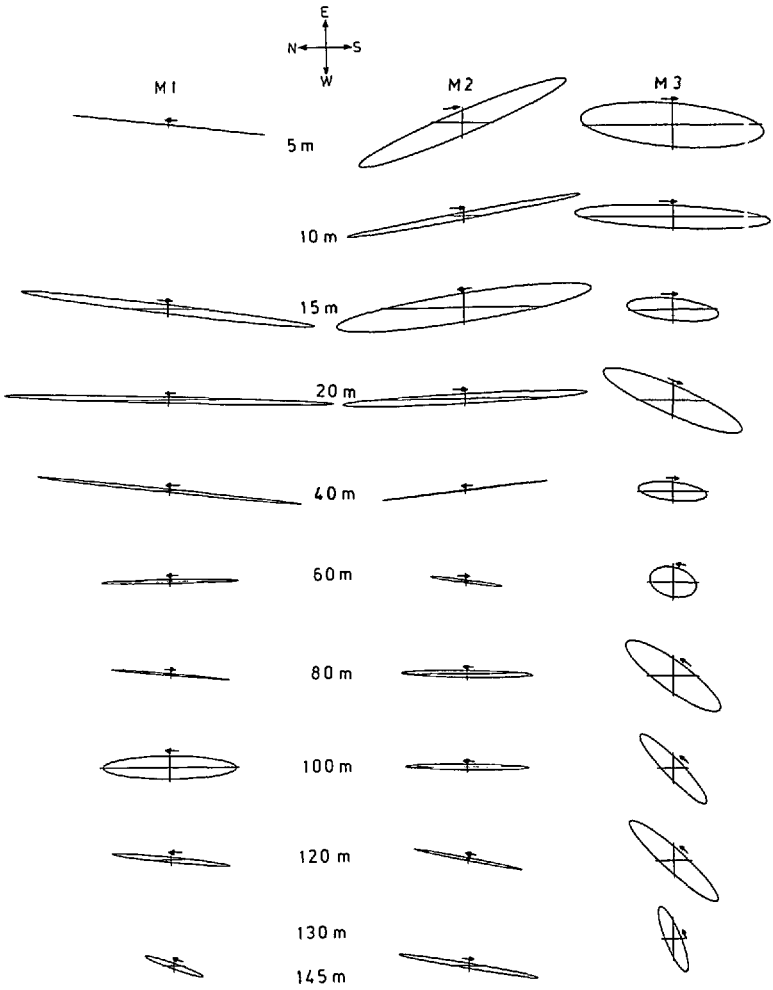

Figure 4. Semidiurnal tidal ellipses calculated from time series of the horizontal velocity components at each current meter. The depths where the current meters were situated are indicated.

system and lengths proportional to the energy in the ellipses. If time is thought to evolve counterclockwise with one cycle corresponding to one tidal period, the angles plotted in the coordinate system then indicate at what time the maximum positive velocity in the tidal ellipse occurs at each depth. A striking feature in Figures 5a,b, and c is the large phase difference between the waves above and those below sill level (60 m). This phase difference ranges from ½ to ¾ of the tidal period. The scenario is as follows: After some time of inflow in the upper part of the water column, a countercurrent builds up in the lower part, and this lower-layer flow reverses some time after the flow in the upper layer has reversed. This indicates the presence of

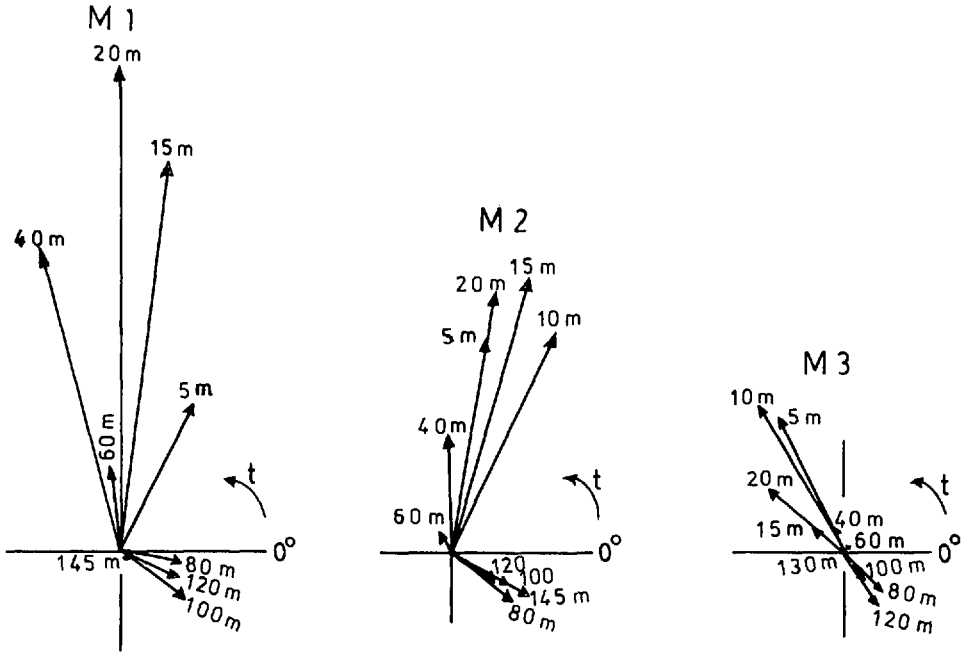

Figure 5. Greenwich phase lags of the tidal ellipses at each depth along the three moorings. Time is evolving counterclockwise, and the lengths of the line segments indicate the energy in the semidiurnal internal tide.

more than one mode in the wavefield; otherwise, the phase difference would have been one half of the tidal period. The plots also suggest a propagation of energy in-fjord from the sill toward both the surface and the bottom, which is in agreement with the ray theory (Cushman-Roisin and Svendsen, 1983). An analogous situation is not uncommon in the open ocean in the vicinity of the shelf break (deWitt *et al.*, 1986).

4. Application of the model to the Skjomen Fjord

The profile of the Brunt-Väisälä frequency, $N(z)$, used in the model is calculated from an average of the density profiles obtained from the hydrographical data in Skjomen Fjord. This profile is then smoothed. Since measurements below 90 meters are scarce, the Brunt-Väisälä frequency is extrapolated there at a constant value equal to 0.0075 s^{-1}. The resulting profile is displayed on the left side of Figure 3.

Using the frequency $\omega = 1.405 \times 10^{-4}\ s^{-1}$ for the M_2-tide (12.42 hrs.), the profile of the ray-slope parameter $c(z) = \omega/N(z)$ is formed, and the integration

$$\zeta = \int_o^z \frac{dz'}{c(z')}$$

is performed to define the new vertical variable. Uniform grid steps have equal lengths in the x and ζ coordinates to guarantee that the rays follow the diagonals of the grid, and a grid-step of $\Delta = 400$ m is chosen to form a grid-mesh of 71 horizontal steps and 54 vertical steps. The even grid-steps in ζ correspond to uneven steps in the physical z-axis, varying from 0.5 meters near the top where $N(z)$ is largest, to 7.5 meters in the deepest region where $N(z)$ is smallest (left side of Fig. 3). Solid boundaries must be stepwise and are chosen to make the best fit to the topography. The resulting grid had 1436 unknown values of u and w. By tracing rays from grid point to grid point, it can be seen that, for this particular choice of stratification and topography, most of the rays are connected with the entrance area, so resonance is weak (Cushman-Roisin *et al.,* 1989). The longest possible time step is found to be $\Delta t = \Delta^2/2$ to keep the iterations of this particular case stable. The numerical relaxation procedure is accelerated by decreasing the value of λ (the diffusion parameter) during the run, from an initial value of $\Delta^2/2$ down to $\Delta^2/3$. The number of iterations needed to get a cumulated mass imbalance of less than one percent is 235,158 (Cushman-Roisin *et al.,* 1989). The residual R that measures the departure in χ and ϕ from zero (Cushman-Roisin *et al.,* 1989) has then dropped from an initial value of 7730.0 to $2.01 \cdot 10^{-7}$. [Another method of accelerating the relaxation has also been found useful: using two alternating time steps, one large and one small such that the double step is numerically stable. Tests indicate that this Chebyshev-acceleration method can reduce the number of iterations, in the present case, by 37%.]

From the velocity field (u,w) returned by the model, the streamfunction $Re[\psi \exp(-i\omega t)]$ is calculated. Contours of the streamfunction are displayed on Figure 6 as the tide proceeds. These plots clearly show two branches in the wave field, both originating at the sill, with one propagating toward the surface and the other toward the bottom. Between them is a shadow zone with almost no flow. Such branching is found in the present data set (Figs. 4–5), and had already been found in earlier data (Cushman-Roisin and Svendsen, 1983). The streamfunction patterns also reveal that there is a phase lag between the two branches, with the upper branch leading the lower, in qualitative agreement with the phase difference found in the data (Fig. 5).

It is possible to make quantitative comparisons between the energies and phases predicted by the model and those found in the data. Because the data are limited to horizontal velocities, only the horizontal velocities of the model are considered, defined as $u(x,z,t) = Re\{[u_R(x,z) + iu_I(x,z)]e^{-i\omega t}\} = u_R(x,z)\cos\omega t + u_I(x,z)\sin\omega t$, where u_R and u_I are respectively the real and imaginary parts of the horizontal velocity output by the model, and ω is the tidal frequency. This expression is of course horizontally one-dimensional, leading to perfectly elongated ellipses with the two extreme values occurring when the phase ωt satisfies the equation $\tan\omega t = u_I/u_R$. Note that, in the present notation, $\omega t = 0$ corresponds to the maximum of the vertical

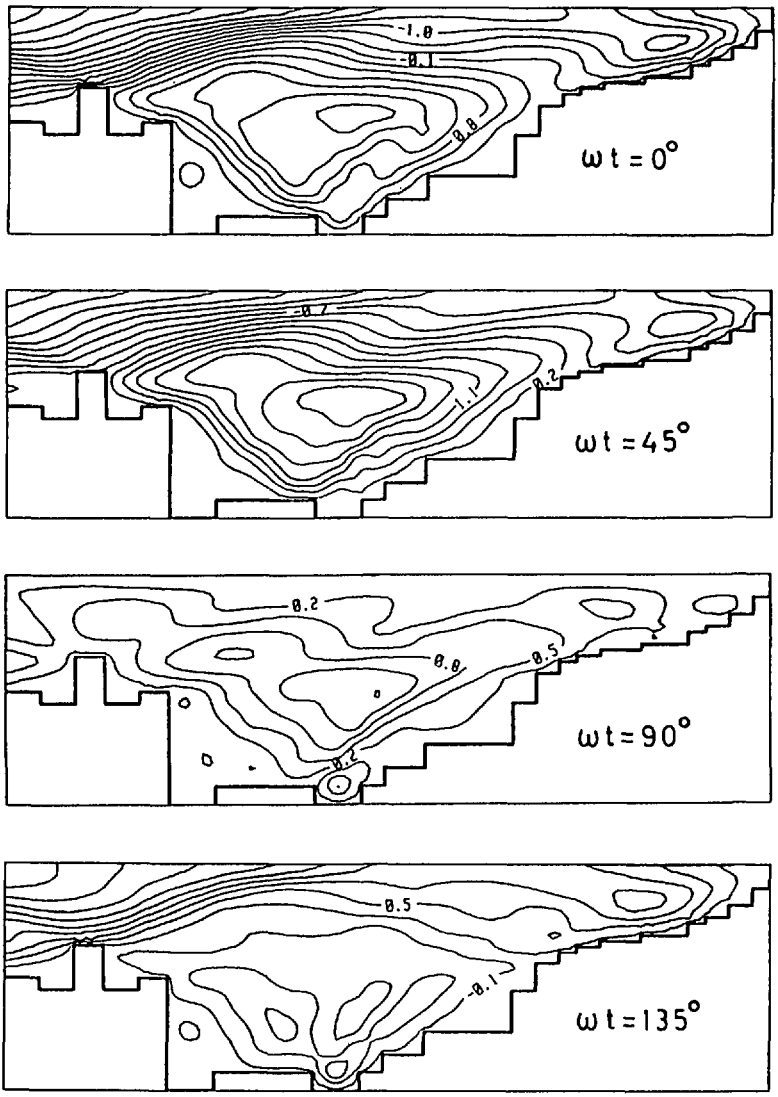

Figure 6. Streamfunction during the first half of the tidal period obtained by the model of Skjomen Fjord.

velocity at the entrance of the fjord (mid point between low and high tides) and thus also to the reference phase used in the data analysis. A convenient way to define the phase lag at a specific position (x_i, z_i) is therefore to take the phase ωt at which $u(x_i, z_i, t)$ reaches its positive extreme value. It follows that the phase lag is the angle of the vector $[u_R, u_I]$ in the complex plane. In analogy with the estimation of the energy levels from the data, the simulated energy levels are taken as $u_R^2 + u_I^2$. The velocities are rescaled to physical magnitudes, based on an amplitude of the surface

tide equal to 1.0 meter, according to observations. Although the wave energy is not strictly the velocity square, this representation is sufficient for the purpose of comparing the energy levels between model and data.

The three columns of the numerical grid corresponding to locations nearest to the three mooring lines were then selected: columns 17, 22 and 27 to represent moorings M1, M2 and M3, respectively. Because of the staggered nature of the grid, the model calculates horizontal velocities only along even-numbered columns. Therefore, we linearly interpolated the u velocities of adjacent columns to estimate their values at columns 17 and 27. Also, because the two-dimensionality of the model does not take into account variations in the fjord's width, a correction was applied. To conserve mass, the flow naturally accelerates and decelerates according to the variations in the cross-sectional of the fjord. Therefore, we multiplied the u-velocities of column n by the area ratio A/A_n, where $A = 17 \times 10^4$ m^2 is approximately the average cross-section in the vicinity of the moorings, and $A_{17} = 7 \times 10^4$ m^2, $A_{22} = 13 \times 10^4$ m^2 and $A_{27} = 15.6 \times 10^4$ m^2 are the actual cross-sections at the three mooring locations, M1, M2 and M3, respectively. From the complex u-velocities so obtained, energies and phases were then calculated. Comparisons between model results and observations are presented on Figure 7a, 7b and 7c for the three mooring locations.

The top panels of each of the three figures compare the simulated (curves) and observed (dots) energy levels, defined as the square of the horizontal-velocity maximum during the tidal cycle. In the upper level (above 60 meters), the vertical distribution of wave energy is correctly reproduced by the model at all three mooring locations. The substantial decrease of energy from mooring M1 to mooring M2 is also correctly modeled. At mooring M2 (Fig. 7b), the model slightly underestimates the energy level, while it overestimates the energy level at mooring M3 (Fig. 7c) by as much as 30%. This last discrepancy may be attributable to the complex geography of the fjord in the vicinity of mooring M3 (Fig. 2); the sharp elbow in the fjord shape and the complicated bathymetry make it difficult to apply a precise cross-section correction factor. Also, the shallow bank on the east side and down-fjord from the mooring (top of Fig. 2) may reflect or break waves so that a portion of the original wave energy may never reach mooring M3. [In retrospect, mooring M3 was not ideally positioned to test a two-dimensional model.]

At all three mooring locations, the model yields a level of minimum energy at about 60 meters. This is in total agreement with the observations. Furthermore, the model provides the explanation. As discussed earlier, it is readily apparent from Figure 6 that the internal tides are prefentially generated at the inward sill edge and that from this location emanate two energy beams, one upward and the other downward. Consequently, further in-fjord, there is a shadow zone at approximately the sill level.

Below the sill level, the model reproduces the secondary energy maximum at all three moorings, but the amplitudes (except for a sharp peak in the profile of column

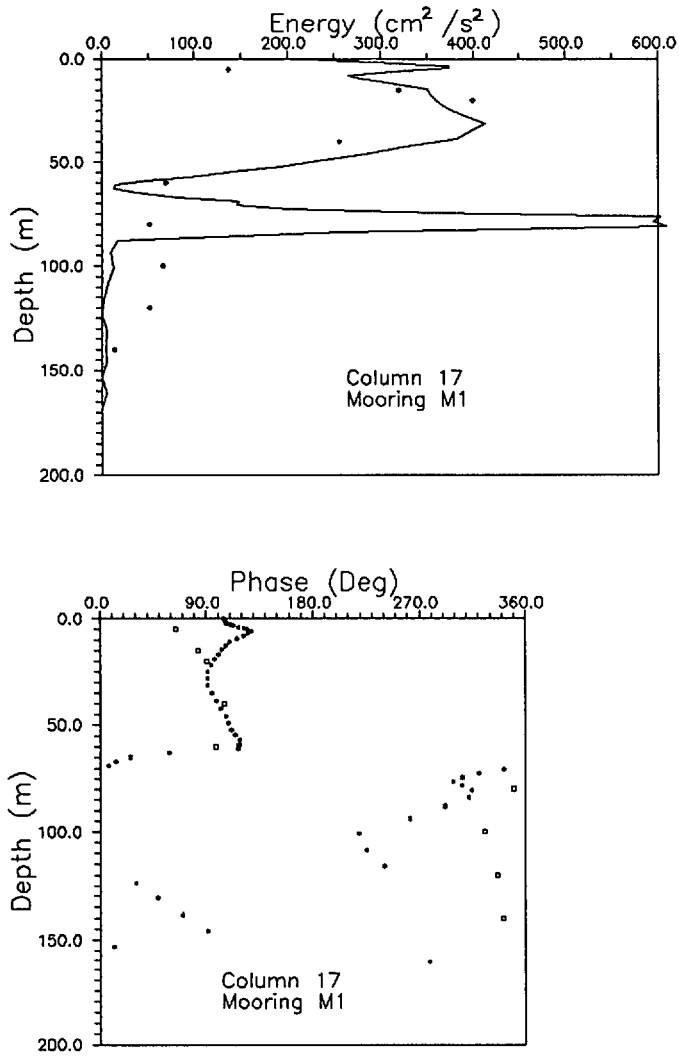

Figure 7a. Top panel: The energy profile $(u_R^2 + u_I^2)$ according to column 17 of the model, corrected for the varying width of the fjord (see text); dots indicate the observed energy levels at mooring M1. Bottom panel: simulated (stars) and observed (open squares) phases for column 17 of model and M1 mooring data, respectively.

17, nearest to mooring M1) are underestimated, and the depths are somewhat off. One possible reason for these discrepancies may be that the Brunt-Väisälä frequency value assumed for the model below 90 meters in the absence of data is inaccurate.

Whatever the difference is between data and model, it is clear that the lower, downward propagating beam is substantially less energetic than the upward-propagating beam. This observation contrasts with the typical situation at the

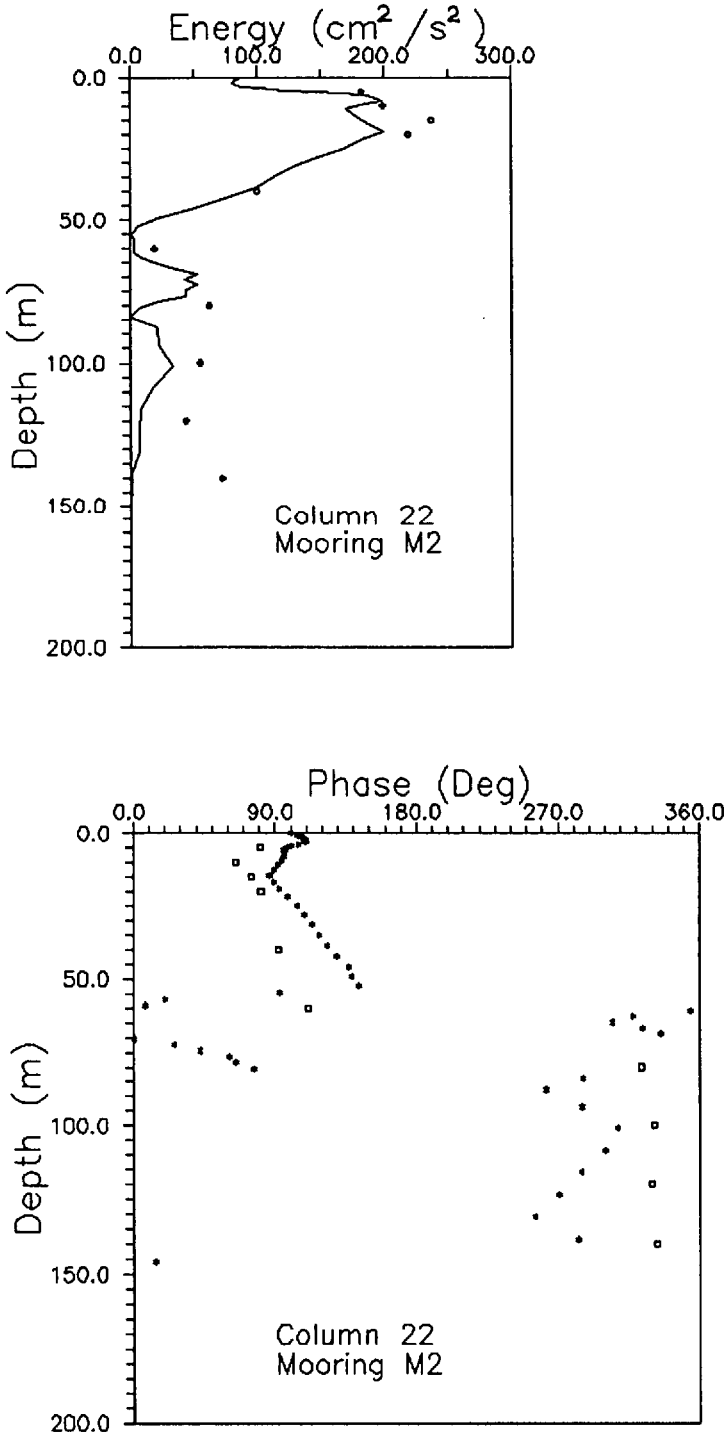

Figure 7b. Same as Figure 7a but for column 22 of the model and data from mooring M2.

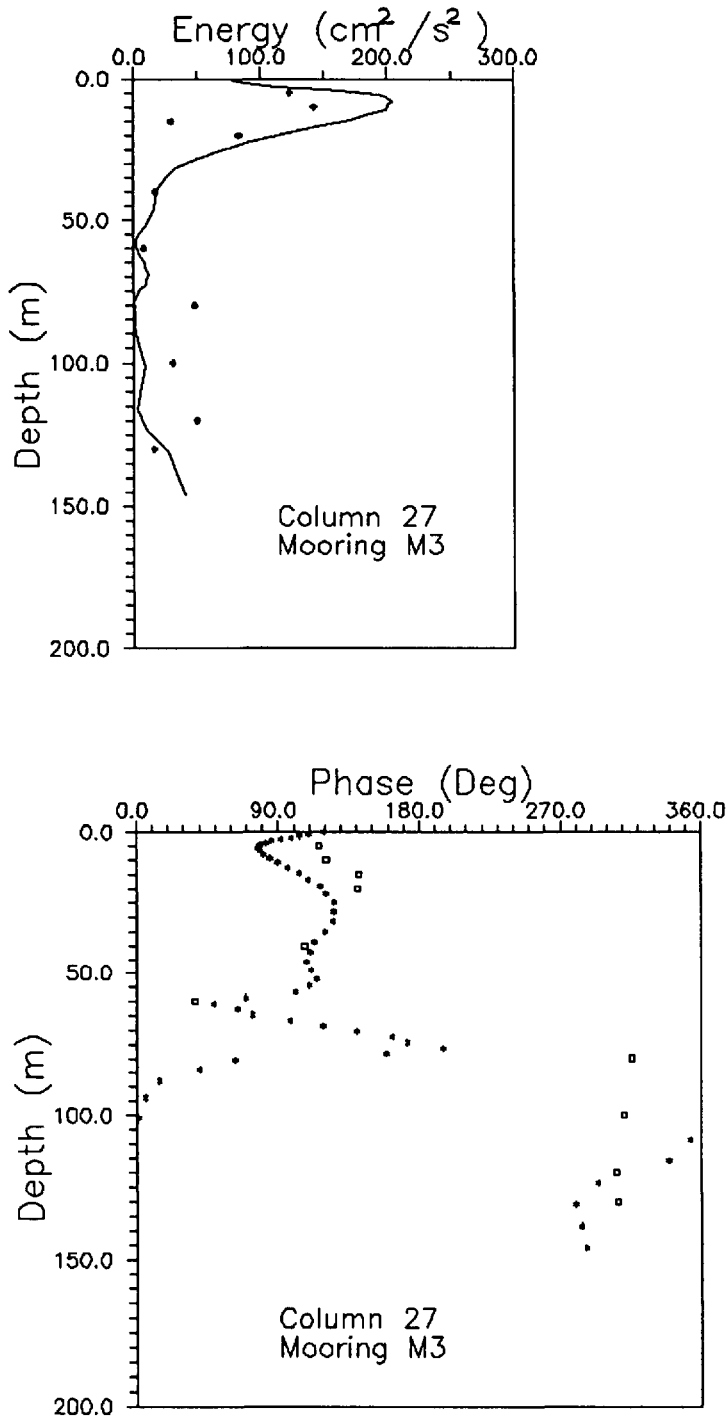

Figure 7c. Same as Figure 7a but for column 27 of the model and data from mooring M3.

continental shelf break where the lower beam is usually the most energetic of the two (deWitt *et al.,* 1986; New and Pingree, 1990).

The bottom panels of Figure 7a, 7b and 7c compare the simulated (stars) and observed (open squares) phases at the three mooring locations. In discussing phases, one must bear in mind the energy levels, for phases become uncertain and meaningless at low energy levels. The streamfunction plots (Fig. 6) and the previous discussion of energy profiles (top panels of Figs. 7) reveal two beams emanating from the sill: one broad and energetic beam propagates upward, and the other, narrower and weaker, propagates downward. One expects the phases of these two beams to be quite different, and they indeed are. At the core of the upper, most energetic beam, the simulated phases are in excellent agreement with the observations. In particular, the variation of phase with depth across the beam is correctly reproduced at all three mooring locations. [The good agreement at mooring M3 may in fact be fortuitous, given the complex situation at that location.] The change in phase from one mooring to the next is also accurately simulated: both data and model indicate a phase lag of about 10 degrees from mooring M1 to mooring M2, although the simulated phases are behind the observed ones at each location. Physically, the energy is propagated in-fjord.

The lower beam appears narrower in the model and broader in the observations, but both model and data agree on the basic trends. As the beam extends in-fjord, its depth increases and phase decreases, from approximately 80 m and 310°–350° at mooring M1/column 17, to 100 m and 280°–310° at mooring M2/column 22, and finally to 150 m and 280°–290° at mooring M2/column 27.

The most striking feature in both simulated and observed phases is the pronounced phase shift between the upper and lower beams, which was not readily apparent from the streamfunction plots (Fig. 6). According to Figures 7a, b, c, the lower beam lags behind the upper beam by at least half a cycle, about 180° according to the model, and about 230° according to the data. Because an exact 180° shift would correspond to a first baroclinic mode, it can be concluded that the model tends to exaggerate the relative importance of this mode.

The very pronounced peak in column 17 of the model at a depth of about 80 meters (Upper panel of Fig. 7a) requires special attention. Undoubtedly, it is attributed to the sharp edge of the sill only two gridpoints away (Fig. 3). At first, one might conclude it an artifact of the numerical solution. Because the inner shoulder is in reality a little deeper than its model representation (87 m instead of 80 m), a velocity peak in the data, if one exists, should be detected around 85–90 meters. Unfortunately, no current meter was placed at such depth, and the depths of the nearest current meters, 80 and 100 meters, were presumably too distant to capture this thin beam.

Fortunately, the four CTD stations taken in the vicinity of moorings M1 and M2 (see Section 3b) give us, by virtue of their fine vertical resolution, the opportunity to

confirm or disprove the existence of this high-energy beam. Our conjecture is that if the beam exists, its high amplitudes should cause wave breaking and thus leave traces of vertical mixing in the vicinity of the sill shoulder. Because salinity is here the main contribution to density variations, we choose to concentrate on the salinity profiles of the CTD casts. The pycnocline extending from sill depth (60 m) to the depth of the inner shoulder (87 m) and overlying the rather homogeneous deep waters (Fig. 3) corresponds to a halocline with a salinity ranging from 32.4 to 33.8 parts per mil. Figures 8a and b show the salinity profiles at the mooring locations M1 and M2, respectively. Also, each figure displays two profiles, taken at different phases during the tidal cycle. If the model is correct and the high-energy beam is present at M1 but not at M2, then mixing should be detected at depths around 80–90 m in Figure 8a and not in Figure 8b. Indeed, the profile at station 99 (Fig. 8a) indicates a breakdown of the sharp transition (rounding of the corner) which may well have been caused by a mixing event. Furthermore, at the same location but several hours later (Station 109), the shape of the transition zone has been substantially changed, indicating additional mixing in the intervening time. By contrast, there is no such indication of mixing at M2 (Fig. 8b).

5. Conclusions

A two-dimensional numerical model of tide-generated internal gravity waves above arbitrary topography, developed by Cushman-Roisin *et al.* (1989), has been generalized. Two major extensions are the allowance for an arbitrary vertical stratification and a radiation condition along the open boundary. The first change involves the use of a density-dependent vertical variable, which is equivalent to using a grid stretched so that its diagonal directions are aligned with the characteristic directions of the waves. The radiation boundary condition is imposed by coupling the two columns closest to the open boundary via an outer solution consisting of normal modes. This involves a computation of a discretized solution of the normal modes for the actual stratification in the domain.

Data collected in the Skjomen Fjord in North Norway show evidence of internal waves with the frequency of the semi-diurnal tide. Tidal ellipses and Greenwich phase lags are calculated from the one-month long time series of current measurements. The wave energy is strongest in two regions, above and below sill level, leaving a region of low energy at sill level. The energy diminishes inward, partly due to a widening of the fjord and, perhaps also, partly due to sideways energy losses. Finally, a phase lag between the two energy bands, above and below sill level, of more than half the tidal period is noted.

Based on hydrographical data, a representative density profile for the fjord is calculated, and a stretched grid is constructed. The model streamfunction reproduces the two branches evolving from the sill, one toward the surface and the other toward the bottom, in excellent agreement with the data. Furthermore, the com-

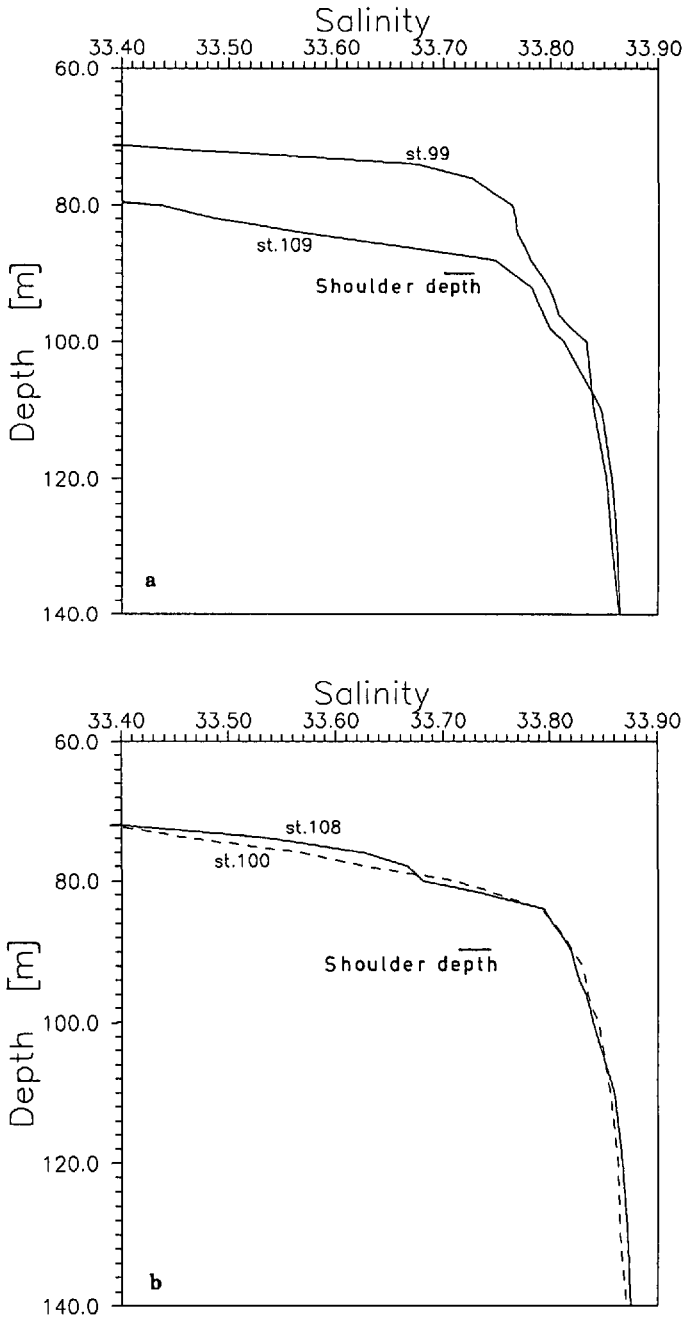

Figure 8. Segments of salinity profiles taken Sept. 6, 1983, showing the transition zone between the halocline and the deep water masses (a) in the vicinity of mooring M1 (CTD-stations 99 and 109 taken at 12:05 and 19:05, respectively) and (b) in the vicinity of mooring M2 (CTD-stations 100 and 108 taken at 12:20 and 18:50, respectively).

puted phase difference between these two branches is in very good agreement with the corresponding phase difference found in the data. When the computed velocity field is corrected for the widening of the fjord, the model energy decreases in-fjord, in a manner consistent with the decrease found in the data. Finally, a very narrow energy beam is predicted by the model. Because the current meters were placed too far apart, there is no trace of such a beam in the current data, but an examination of the salinity profiles do reveal a zone of mixing at approximately the right depth in the vicinity of the sill shoulder and suggests that such a high-energy beam does exist and is responsible for some wave breaking and vertical mixing.

The model described here is sufficiently general to be applicable to various systems, not only constricted water bodies such as fjords but also open coastal areas such as shelf and slope. Because it is built to handle resonance, the model is also apt to provide accurate descriptions of the energy distribution in resonant fjords (Lewis and Perkin, 1982; de Young and Pond, 1987).

Acknowledgments. The authors would like to thank Dr. Patrick Gaffney and his team at the Bergen Scientific Centre for their support and access to the IBM computing facilities. Pertinent comments and useful references provided by Dr. Dong-Ping Wang are gratefully acknowledged. The Office of Naval Research of the USA also supported the second author during part of this research.

REFERENCES

Aanderaa Instruments. 1979. RCM 4/5. Recording current meter models 4 & 5. Technical description, No. 119.

Baines, P. G. 1971. The reflection of internal/inertial waves from bumpy surfaces. J. Fluid Mech., *46,* 273–291.

—— 1974. The generation of internal tides over steep continental slopes. Phil. Trans. R. Soc. London, *277A,* 27–58.

Buckley, J. R. 1980. A linear model of internal tides in fjords, *in* Fjord Oceanography, Freeland, Farmer and Levings, eds., Plenum Pub., 165–171.

Chuang, W.-S. and D.-P. Wang. 1981. Effects of density front on the generation and propagation of internal tides. J. Phys. Oceanogr., *11,* 1357–1374.

Craig, P. D. 1987. Solutions for internal tidal generation over coastal topography. J. Mar. Res., *45,* 83–105.

—— 1988. A numerical model study of internal tides on the Australian Northwest Shelf. J. Mar. Res., *46,* 59–76.

Cushman-Roisin, B. and H. Svendsen. 1983. Internal gravity waves in sill fjords: Vertical modes, ray theory and comparison with observations, *in* Coastal Oceanography, H. Gade *et al.,* eds., Plenum Pub. Corp., 373–396.

Cushman-Roisin, B., V. Tverberg and E. G. Pavia. 1989. Resonance of internal waves in fjords: A finite-difference model. J. Mar. Res., *47,* 547–567.

deWitt, L. M., M. D. Levine, C. A. Paulson and W. V. Burt. 1986. Semidiurnal internal tide in JASIN: Observations and simulations. J. Geophys. Res., *91,* 2581–2592.

de Young, B. and S. Pond. 1987. The internal tide and resonance in Indian Arm, British Columbia. J. Geophys. Res., *92,* 5191–5207.

Gardner, W. D. 1989. Periodic resuspension in Baltimore Canyon by focusing of internal waves. J. Geophys. Res., *94,* 18185–18194.

Godin, G. 1972. The Analysis of Tides, University of Toronto Press, Toronto, 264 pp.

Golubev, Yu. N. and L. V. Cherkesov. 1986. Internal waves with tidal periods above a local bottom rise. Izv. Atmos. Ocean. Phys., *22*(7), 607–608 (English translation).

Hibiya, T. 1986. Generation mechanism of internal waves by tidal flow over a sill. J. Geophys. Res., *91,* 7697–7708.

—— 1988. The generation of internal waves by tidal flow over Stellwagen Bank. J. Geophys. Res., *93,* 533–542.

Lewis, E. L. and R. G. Perkin. 1982. Seasonal mixing processes in an Arctic fjord system. J. Phys. Oceanogr., *12,* 74–83.

Lighthill, J. 1978. Waves in Fluids, Cambridge University Press, 504 pp.

McCalpin, J. D. 1990. The design and implementation of a three-dimensional, primitive equation ocean circulation model. Ph.D. dissertation, Florida State University, Tallahassee, Florida, 160 pp.

New, A. L. 1988. Internal tidal mixing in the Bay of Biscay. Deep-Sea Res., *35,* 691–709.

New, A. L. and R. D. Pingree. 1990. Large-amplitude internal soliton packets in the central Bay of Biscay. Deep-Sea Res., *37,* 513–524.

Pingree, R. D. and A. L. New. 1989. Downward propagation of internal tidal energy into the Bay of Biscay. Deep-Sea Res., *36,* 735–758.

Prinsenberg, S. J. and M. Rattray, Jr. 1975. Effects of continental slope and variable Brunt-Väisälä frequency on the coastal generation of internal tides. Deep-Sea Res., *22,* 251–263.

Rattray, M., Jr. 1960. On the coastal generation of internal tides. Tellus, *12,* 54–62.

Sandstrom, H. 1976. On topographic generation and coupling of internal waves. Geophys. Fluid Dyn. *7,* 231–270.

Vlasenko, V. I. 1987. Internal wave generation in a stratified ocean of variable depth. Izv. Atmos. Ocean. Phys., *23*(3), 225–230 (English translation).

Wunsch, C. 1969. Progressive internal waves on slopes. J. Fluid Mech., *35,* 131–144.

Received: *9 October, 1990;* revised: *20 June, 1991.*